Mass transfer and hydrodynamic characterization of structured 3D electrodes for electrochemistry

Mass transfer and hydrodynamic characterization of structured 3D electrodes for electrochemistry

Jonas Hereijgers[1, *], Jonathan Schalck[1], Tom Breugelmans[1, 2]

[1] *Research group Applied Electrochemistry & Catalysis, University of Antwerp, Universiteitsplein 1, 2610 Wilrijk, Belgium*
[2] *Separation & Conversion Technologies, VITO, Boeretang 200, 2400 Mol, Belgium.*

*Corresponding author: tel. (+) 32/ 3.265.23.48, e-mail: jonas.hereijgers@uantwerp.be

Abstract

Electrochemical reactors are more and more equipped with 3D electrodes such as foams and felts instead of flat electrodes, because of their large surface area and ability to reduce mass transfer limitation. Being a surface process, mass transfer limitation in electrochemical reactors limits productivity and can even result in unwanted side reactions. While 3D electrodes such as foams and felts are a significant improvement, they come with a high operating cost in terms of pumping power. Its irregular shape inflicts pressure drops three to four orders of magnitude higher than an open conduit equipped with a flat electrode. In this work we present structured 3D electrode designs derived from static mixers. Intended to maximize mass transfer at a minimal pressure drop these static mixer-derived electrodes result in similar mass transfer performance and hence electrochemical behavior as the commercial felt electrodes, but at a pressure drop that is two orders of magnitude lower. Due to their regularly structured design with a focus on minimal pressure drop these electrodes surpass the current state-of-the-art felt electrodes.

Keywords

3D electrode; mass transfer; additive manufacturing; electrochemical reactor; electrochemistry; redox flow battery

List of symbols and abbreviations

k_m	mass transfer coefficient (m s^{-1})
A_e	volumetric active area of the electrode (m^2/m^3)
$k_m A_e$	volumetric mass transfer coefficient (s^{-1})
I_{lim}	limiting current (A)
n	number of transferred electrons (-)
F	Faraday constant (A s mol^{-1})
V_e	electrode volume (m^3)
C_{bulk}	concentration of ferricyanide in the bulk phase (mol m^{-3})
ν	mean linear electrolyte velocity (m s^{-1})
Q	flow rate (m^3 s^{-1})
ε	volumetric porosity (-)
d_h	hydraulic diameter (m)
A_x	cross-sectional area of the channel (m^2)
$A_\perp$	cross-sectional area of the electrolyte flow (m^2)
$P_\perp$	wetted perimeter of the cross-section of the electrolyte flow (m)
μ	dynamic viscosity of the electrolyte (Pa s)
γ	energy dissipation rate (W kg^{-1})
ΔP	pressure drop (Pa)
ρ	density of the electrolyte (kg/m^3)
V_f	volume of the electrolyte (m^3)
D_m	molecular diffusion coefficient (m^2/s)
Re	Reynolds number
Sc	Schmidt number

Sh	Sherwood number
α_1	empirical variable Eq. 6
α_2	empirical variable Eq. 6
β_1	empirical variable Eq. 6
β_2	empirical variable Eq. 6
a_1	empirical variable Eq. 7
a_2	empirical variable Eq. 8
a_3	empirical variable Eq. 11
b_1	empirical variable Eq. 7
b_2	empirical variable Eq. 8
b_3	empirical variable Eq. 11
RLPD	Ross low pressure drop
SMX	Sulzer mixer
H	Horizontal
V	Vertical
CW	Clockwise
CCW	Counter-clockwise

1. Introduction

With the growing awareness towards climate change, society is in search of green technologies to replace current fossil fuel-based processes. The industrial electrification fits seemingly in this quest. Using electrochemistry, industrial chemical processes can make the shift from fossil energy sources to renewable ones. In electrochemistry electrons drive the reaction rather than heat and pressure. Consequently, electrochemical reactors can operate at ambient conditions. Being a surface process, the reagents in electrochemistry has to be transported towards the electrode. The majority of the electrochemical reactors are of the filter-press type and hence are equipped with planar electrodes, such as water electrolyzers, chlor-alkali reactors and fuel cells [1–7]. In such filter-press type electrochemical reactors the electrolyte flows alongside the electrode. This results in the formation of a concentration depleted diffusion layer near the vicinity of the electrode surface, causing mass transport limitation at high current densities, also known as the limiting current density. In this mass transport limited regime an increased overpotential can lead to unwanted side reactions such as hydrogen or oxygen evolution, typically observed when operating in galvanostatic mode [8]. Depletion of the electroactive specie at the electrode surface, will then result in a higher cell potential to uphold the requested current, causing unwanted side reactions to appear. To reduce the diffusion layer at the electrode and increase productivity, the electrochemical reactor is often fitted with turbulence promotors or equipped with flow distributing bipolar plates [3,9–11]. These flow guiding structures increase the velocity, enhancing mass transfer properties, but also reduce the channel dimensions, increasing pressure drop without increasing the electrode surface.

Alternatively, 3D electrodes such as foams and felts are more and more used as electrodes in electrochemical reactors for various purposes such as redox flow cells, corrosion and

electrodeposition, metal ion removal, organic oxidation of wastes and electrochemical synthesis [12]. Because their surface area is one to several orders of magnitude larger than that of a planar electrode, mass transfer limitation can largely be neglected and the limiting current density increased. 3D electrodes such as foams and felts are irregularly shaped. This irregular shape results in increased surface area, tortuosity and channeling effects, which is known to adversely affect the pressure drop [13,14]. As a result felt electrodes report pressure losses up to 1 bar depending on the flow path length [15]. Bryans et al. evaluated a 200 kW redox flow battery stack equipped with felt electrodes and characterised its overall energy loss [16]. For a charge/discharge power usage of 100 kW and 200 kW, roughly 8 kW of pumping power was required, resulting in a 4-8 % overall power efficiency loss.

To diminish pressure losses, flow guiding structures have been combined with foams and felts (e.g. interdigitated channels) [12]. Traditionally, tools like CNC machining and injection molding has been used to fabricate these flow guiding structures. With the rise of 3D printing the last decade, improved manufacturing tools have become available [17,18]. Using 3D printing, reactor bodies with a higher degree of complexity can be fabricated, such as labyrinthine pathway manifolds preventing shunt or by-pass currents between adjacent cells [18]. Initially the printable materials were restricted to polymers. Nowadays also metals such as nickel, copper, iron, stainless steel and titanium alloys can be printed by laser techniques, although at a fairly high cost [19]. This allows to not only print complex reactor bodies, but also regularly shaped 3D electrodes. Using selective laser melting we demonstrated in a proof-of-concept the impact a structured 3D electrode can have on the mass transport properties and electrode surface area. By printing a turbulence promotor in stainless steel and by using it as electrode, the mass transfer coefficient was increased with 76 % compared to the filter-press type reactor [20]. The combination of electrode and turbulence promotor

resulted in shear forces at the electrode-electrolyte interface, lowering the thickness of the diffusion layer yielding the observed mass transfer improvement. Arenas et al. demonstrated that porous electrodes develop higher current densities, discouraging the use of planar electrodes [15,21]. The examined structured 3D electrodes, however, were restricted to turbulence promotor-derived designs such as Pt/Ti meshes. Consequently, the pressure drop at comparable mass transport coefficients was similar and in the same order of magnitude to that of irregular shaped 3D electrodes such as felts. To have a substantial impact on the pressure drop, while maintaining the same mass transport properties, alternative electrode designs than turbulence promotor-derived ones are required.

An optimal electrode design has the characteristics of effective electrolyte transport, high conductivity, stable three-dimensional network structure, large surface area and good (electro)chemical stability [22]. In this regard, static mixers hold interesting properties. Trying to mix fluids, likewise, requires high mass transport rates and similarly aims at minimizing pressure drop. Hence, static mixer designs are highly interesting as geometry for structured 3D electrodes. Static mixers consist of repetitive stationary unit cells that induce motion in the flowing fluid that is function of the unit cell design. Each unit cell divides the flowing fluid into regions that are rotated and then recombined at the end of the unit cell, where the next unit cell divides the flow again. Several unit cell designs exist, however, the three most common mixer unit cells are, Kenics mixer, Ross Low-Pressure Drop mixer (RLPD) and Sulzer mixer (SMX) [23,24].

In this work, we show that structured 3D electrodes derived from static mixer unit cell designs outperform the frequently used commercial felt electrode with two orders of magnitude regarding pressure drop while maintaining similar mass transfer properties. Through rapid-

prototyping and experimental characterization using the limiting current technique the electrode design was optimized.

2. Material and methods

2.1 Chemicals

Potassium ferricyanide, potassium ferrocyanide, toluene, glycerol and potassium bicarbonate were purchased at Chem-Lab Analytical (Belgium). Nickel powder (< 50 µm, 99.7 %) was obtained from Sigma- Aldrich (Belgium), limosolve from Formfutura (The Netherlands) and epoxy (Specifix 40) from Struers (The Netherlands). All gases were delivered by Nippon Gasses (Belgium). The ultrapure water (18.2 MΩ.cm @25 °C) used throughout the experiments was prepared in the laboratory (Synergy UV, Merck). The Sigracell graphite felt (GFA 6 EA) was purchased at sgl carbon (Germany).

2.2 Electrode fabrication

The 3D electrodes were fabricated according to the indirect 3D printing method [19]. A template of the electrode was printed in limosolve (Ultimaker 3) and subsequently filled with a paste of nickel powder (61.2 wt%), epoxy (14.3 wt%) and glycerol (24.5 wt%). After a curing period of 3 h at 40 °C the template was removed by dissolving the limosolve in toluene. The obtained part, referred to as green part, was subsequently sintered in a two-step process. In the first step the epoxy was removed by heating the green part under air atmosphere (50 mL min^{-1}) according to the following temperature program: (i) temperature was ramped to 300 °C at 5 °C min^{-1}, (ii) once the temperature reached 300 °C it was raised more slowly (1 °C min^{-1}) to 600 °C where it was maintained for 1 h to remove all organic material, (iii) after this 1 h dwell time at 600 °C, the temperature was raised to 1000 °C (1 °C min^{-1}) where it was again maintained for 1 h to sinter the metal particles, and (iv) finally the

temperature was cooled down to room temperature at 1 °C min^{-1}. As this first step proceeded under an oxygen rich atmosphere the nickel was oxidized and hence it was necessary to perform a second reducing step. To this end, the second step was conducted under a 5 % hydrogen in argon atmosphere (150 ml min^{-1}). The nickel oxide was chemically reduced by heating the electrode to 800 °C (1 °C min^{-1}). Once the temperature reached 800 °C it was maintained at 800 °C for 2 h. Next, the electrode was cooled down to room temperate with a rate of 2 °C min^{-1}. This step was repeated twice to ensure the removal of all nickel oxide, which was guaranteed by visual inspection. A cyclic voltammogram test revealed that there was no deactivation of the nickel electrode after this sintering treatment [19]. All electrodes were only used once to determine the limiting current.

2.3 Flow cell configuration

To characterize the mass transfer properties, the 3D electrodes were housed in a custom-made flow cell (Fig. 1). The electrode housing was made out of poly(methyl methacrylate) using a CNC mill (Euromod MP45, Imes). The catholyte and anolyte were separated by a Nafion 117 membrane (Fuel cell store) and sealing was ensured by two viton gaskets. To prevent jet streaming of the entering liquid, a distributor plate with 64 nozzles of 1 mm in diameter was placed in front of the electrode, which was verified through computational simulations [20]. Cathode and anode were connected with a Versastat 3 potentiostat using a nickel wire inserted from the side in a two-electrode configuration (Supporting information, Fig. S5). The flow rate was controlled with a multichannel peristaltic pump (Ismatec, Reglo Digital MS-4/8).

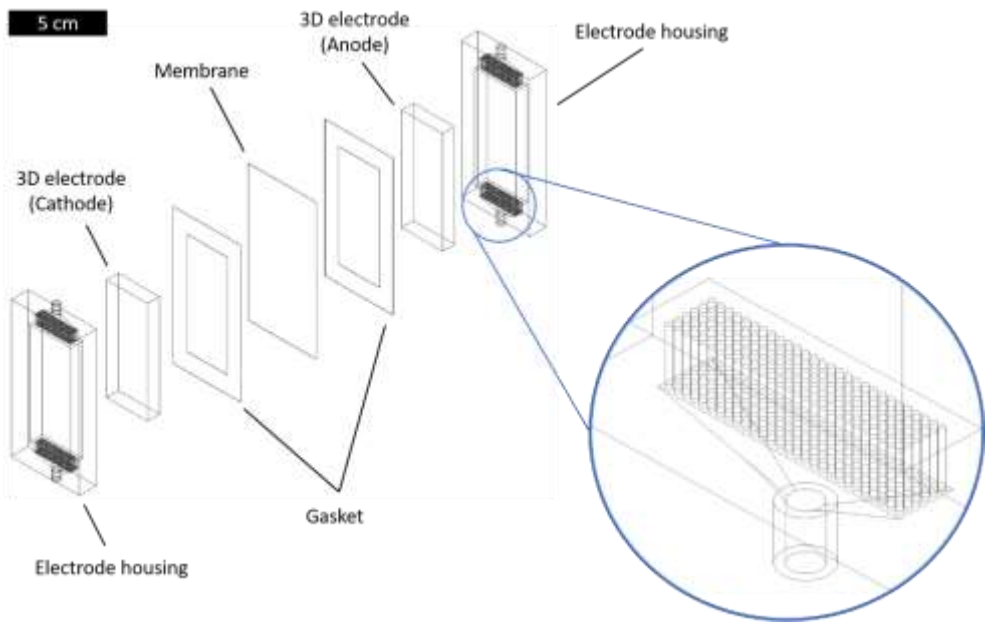

Fig. 1: Scheme of the flow cell and zoom-in of the flow distributor.

2.4 Limiting current technique

Using the limiting current technique [25], the volumetric mass transfer coefficient ($k_m A_e$) was determined under mass transfer controlling conditions for every electrode design at various flow rates (i.e. 15, 22.5, 30, 37.5 and 45 ml min^{-1}). To this end, the reversible reaction of potassium ferrocyanide and potassium ferricyanide was used (Eq. 1).

$$[Fe(CN)_6]^{4-} \rightleftharpoons [Fe(CN)_6]^{3-} + e^- \quad (1)$$

By chronoamperometry the steady-state current response was measured at discrete cell potential values (i.e. 0.2, 0.1, 0, -0.1, -0.2, -0.3, -0.4, -0.5, -0.6, -0.7 V), to ensure that time-based variations in the concentration profile had no impact on the derived limiting current. From the limiting current the product of the average mass transfer coefficient (k_m) and the volumetric active area of the electrode (A_e) was calculated using Eq. 2 [15,25,26].

$$k_m A_e = \frac{I_{lim}}{n\ F\ V_e\ C_{bulk}} \quad (2)$$

Here A_e is the ratio of the electrode surface per electrode volume, I_{lim} the limiting current value, n the number of transferred electrons in the electrochemical reaction, which is one for

the ferri/ferro reaction (Eq. 1), F the Faraday constant, V_e the electrode volume and C_{bulk} the concentration of ferricyanide in the bulk phase. For the structured 3D electrodes V_e was obtained from CAD models (Inventor) and if necessary corrected for any shrinkage caused by the sintering process. For the graphite felt V_e was experimentally measured by determining the volume difference of electrolyte between an empty flow cell and a flow cell equipped with a felt electrode. Specifically for the flat electrode the volumetric active area of the electrode was defined as the active area of the electrode per reactor volume instead of electrode volume as was the case for all other electrodes [27]. This implied that in Eq. 2 V_e was for the flat electrode not the electrode volume but the reactor volume. The limiting current was determined at -0.3 V. The impact of this potential on the mass transfer coefficient was limited, as the limiting current plateau only varied slightly. This effect has been studied in previous work [19].

During measurements the cathode was connected as working electrode and the anode as counter electrode in a two-electrode setup. The catholyte consisted of 25 mM potassium ferricyanide and 0.5 M potassium bicarbonate as supporting electrolyte as it did not interacted with the nickel electrode (see supporting information, Fig. S7). To prevent any limitation effects occurring at the counter electrode the anolyte concentration of potassium ferrocyanide was kept at 100 mM and catholyte and anolyte were pumped in single pass mode through the reactor and discarded thereafter. The potassium bicarbonate concentration was identical to the catholyte, i.e. 0.5 M.

2.5 Hydrodynamics

To gain insight into the hydrodynamic behavior of the structured 3D electrodes computational fluid dynamics (CFD) modelling was performed (Comsol Multiphysics v5.4) using a

computer equipped with an AMD Ryzen 7 2700x processor and 64 GB RAM (DDR4 SDRAM 2666 MHz, Corsair Vengeance LPX). In this case the Navier-Stokes equation for a steady-state incompressible Newtonian flow was solved under laminar flow conditions [28]. As pressure drop values across the structured 3D electrodes were extremely low (< 10 Pa), pressure drop values were taken from the CFD modelling results. To safeguard the accuracy of these simulated pressure drop values, experimental validation was performed. The relative error between the simulated and experimental pressure drop was limited to 6.5 % (see supporting information). The pressure drop across the felt electrode was measured experimentally using a digital pressure sensor (Gefran, TK-series).

The mean linear electrolyte velocity (v), hydraulic diameter (d_h) and Reynolds number (Re) were determined using Eqs. 3-5.

$$v = \frac{Q}{\epsilon A_x} \tag{3}$$

$$d_h = \frac{4A_\perp}{P_\perp} \tag{4}$$

$$Re = \frac{\rho v d_h}{\mu} \tag{5}$$

Here Q is the flow rate, ε the volumetric porosity of the 3D electrode fitted channel, A_x the cross-sectional area of the channel, $A_\perp$ the cross-sectional area of the electrolyte flow, $P_\perp$ the wetted perimeter of the cross-section of the electrolyte flow, ρ the density of the electrolyte and μ the dynamic viscosity of the electrolyte. For the felt electrode an average pore size of 50 µm [29] was taken as the hydraulic diameter. The hydraulic diameter for all other electrodes was calculated using Eq. 4.

3. Results and discussion

3.1 Electrode design

Three classes of structured 3D electrodes were derived from static mixer unit cell designs: (i) Kenics electrodes, (ii) RLPD electrodes and (iii) SMX electrodes (Fig. 2).

Fig. 2: Classes of the structured 3D electrodes: (A) Kenics electrode, (B) RLPD electrode and (C) SMX electrode.

With the used fused deposition modeling 3D printer, the printing resolution was 500 µm. The resolution of course depends on the type of printer and the technology it is based on. Stereolithography 3D printers for instance can achieve resolutions up to 16 µm (e.g. StrataSYS Objet 260). Resolution could be increased by utilizing the shrinkage effect during sintering. Shrinkage was isotropic and was typically 10%. Taking this manufacturing resolution into account [19], five Kenics derived electrodes (i.e. Kenics 1, Kenics HCW/HCW, Kenics HCW/VCW, Kenics HCW/HCCW and Kenics HCW/VCCW), three RLPD derived electrodes (i.e. RLPD 1, RLPD 2 and RLPD 4) and two SMX derived electrodes (i.e. SMX 1 and SMX 2) were developed (see supporting information, Figs. S1-4). The electrode volume and porosity of the structured 3D electrodes is given in Table 1.

Table 1: Geometrical characteristics of the 3D electrodes.

	V_e (cm^3)	ε (%)
Kenics 1	2.56	74.6
Kenics HCW/HCW	3.86	61.7
Kenics HCW/HCCW	3.86	61.7
Kenics HCW/VCW	3.86	61.7
Kenics HCW/VCCW	3.86	61.7
RLPD 1	3.02	70.1
RLPD 2	3.02	70.1
RLPD 4	3.02	70.1
SMX 1	3.86	61.7
SMX 2	6.23	38.2
Felt	2.35	94.0

3.2 Volumetric mass transfer coefficient (k_mA_e)

To calculate the mass transfer coefficient with the conventional limiting current technique the current density must be known [30]. However, determining the electrochemical active surface area of porous electrodes like the felt electrode is near to impossible as it has been shown that surface characterization techniques such as nitrogen sorption overestimates the effective electrochemical active surface area with at least an order of magnitude [31]. Moreover, in scrutinizing different electrode geometries, the size of the electrode surface area is equally important as the mass transfer coefficient, even under mass transfer limiting conditions. A highly efficient electrode geometry in terms of mass transfer properties, but small in electrode surface, will result in a small limiting current and hence small productivity. To this end, multiplying the mass transfer coefficient with the volumetric active area of the electrode

allows to take both parameters (i.e. mass transfer properties and electrode area) into account [15,21,26].

Every time the cell potential changed, the current response was at least ten seconds not constant over time due to a varying concentration profile along the entire length of the 3D electrode (Fig. 3A). Consequently, determining the limiting current by linear scan voltammetry was not feasible. To resolve this problem the cell potential was stepwise varied using chronoamperometric experiments and the current/potential response determined once the current was constant over time. From the resulting polarization curve (Fig. 3B) the limiting current plateau was determined and the mass transfer coefficient determined. An example of such a measurement is given in Fig. 3 for the Kenics 1 electrode. From the obtained polarization curves it can be observed that the limiting current plateau was slightly tilted. This effect has been studied by Newman [32] and can be attributed to side reactions or a non-uniform ohmic potential drop. Since no gas evolution was observed during measurements the occurrence of side reactions was not likely. The electrodes however showed a limited porosity as it exhibited type II physisorption behavior [19]. From porous electrodes it is known that they can exhibit an ohmic potential drop within the pores [33]. Consequently, some regions within the electrode can experience potentials that are less negative and hence produce local currents less than the limiting current, explaining the observed tilted limiting current plateau. When comparing different electrode geometries against one another, this effect can be neglected [19]. These chronoamperometric measurements were repeated at various electrolyte flow rates and for electrode geometries. The reproducibility of these experiments was checked, resulting in a deviation on the limiting current lower than 2.1 %.

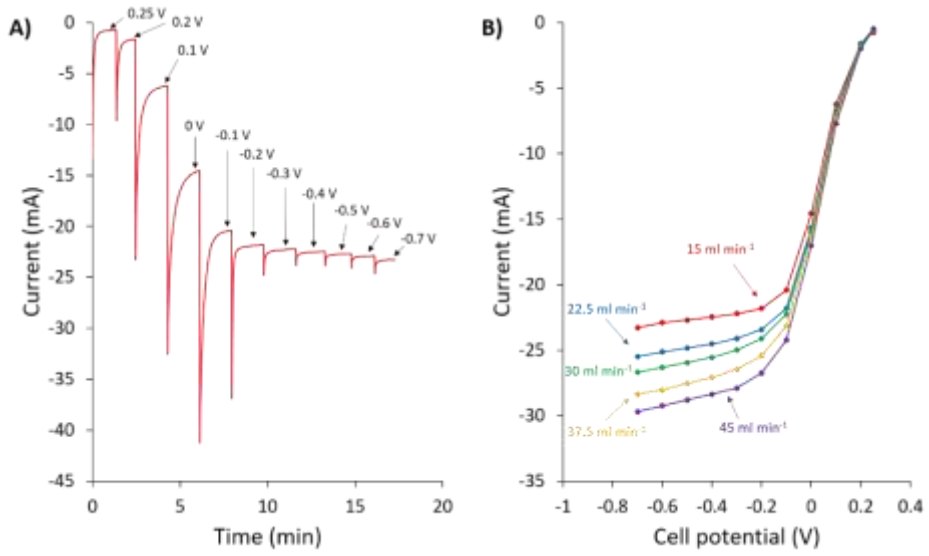

Fig. 3: A) Chronoamperometric measurements of the Kenics 1 electrode at 15 ml min^{-1} at various cell potentials. B) Polarization curve of the Kenics 1 electrode.

From the limiting current the volumetric mass transfer coefficient (k_mA_e) was determined, using Eq. 2. Plotted against the mean linear electrolyte velocity and Reynolds number, it can be observed that for all electrodes the volumetric mass transfer coefficient increased with increasing velocity and Reynolds number (Fig. 4). With increasing velocity the diffusion boundary layer near the electrode surface is known to decrease, increasing mass transfer towards the electrode surface. This behavior was also predicted by Arenas et al. [21] in the form of an empirical power law (Eq. 6).

$$k_mA_e = \alpha_1 v^{\beta_1} = \alpha_2 Re^{\beta_2} \quad (6)$$

Here α_1, α_2, β_1 and β_2 are empirical variables (supporting information, Table S1). Eq. 6 was fitted onto the experimental results in Fig. 4, and is represented by the lines. As the Reynolds numbers were in all measurements below 150, laminar flow conditions applied, as reported critical Reynolds number values were all higher than the ones in this work [34–39]. From the results in Fig. 4 it can be observed that in all circumstances the flat electrode performed inferior compared to any 3D electrode, emphasizing once more the importance of 3D electrodes for electrochemical reactors. However, when comparing the structured 3D

electrodes against the commercial felt electrode it can be seen that only the Kenics HCW/HCCW electrode and in lesser extent the Kenics HCW/VCCW electrode could match the volumetric mass transfer coefficient of the felt electrode. This could be attributed to the additional mixing these Kenics electrodes promotes on the electrode surface due to the formation of periodic flow, which has also been observed in concentric cylinder geometries [40], enhancing substantially the mass transport. This effect most likely is not obtained with the RLPD and SMX electrodes. To achieve the same volumetric mass transfer coefficient than the felt electrode, the mean linear electrolyte velocity with the Kenics HCW/HCCW electrode had to be at least 2.2 times larger compared to the felt electrode. However, the pressure required to attain these velocities can be significantly lower, resulting in a lower total power consumption of the electrochemical reactor [16]. Hence, at equal pumping power cost the electrolyte velocity and therefore also the volumetric mass transfer coefficient can be much higher when using structured 3D electrodes. To this end, the pressure drop across the 3D electrodes was determined as function of the Reynolds number (Fig. 5). From the obtained results it can be seen that the felt electrode caused a pressure drop up to three orders of magnitude larger than the structured 3D electrodes, despite its volumetric porosity being minimum 23.9 % larger than the that of the structured 3D electrodes (Table 1). Consequently, the structured 3D electrodes resulted in a Reynolds number that is several orders of magnitude larger when using the same pumping power. Compared to the flat electrode, the structured 3D electrodes resulted in only a moderate increase in pressure drop. Even dense structures like the Kenics derived electrodes with two layers of helical elements resulted in only one order of magnitude larger pressure drop than the flat electrode. Only the SMX 2 electrode caused a pressure drop that was two orders of magnitude larger than the flat electrode. This was mainly attributed to the much smaller volumetric porosity that was only 38.2 %. Sandoval et al. [41] has shown that the pressure drop is a logarithmic function of the Reynolds number (Eq.)

$$\Delta P = a_1 Re^{b_1} \quad (7)$$

Here a_1 and b_1 are empirical variables. This empirical power law was fitted on the data in Fig. 5 (see supporting information, Table S1).

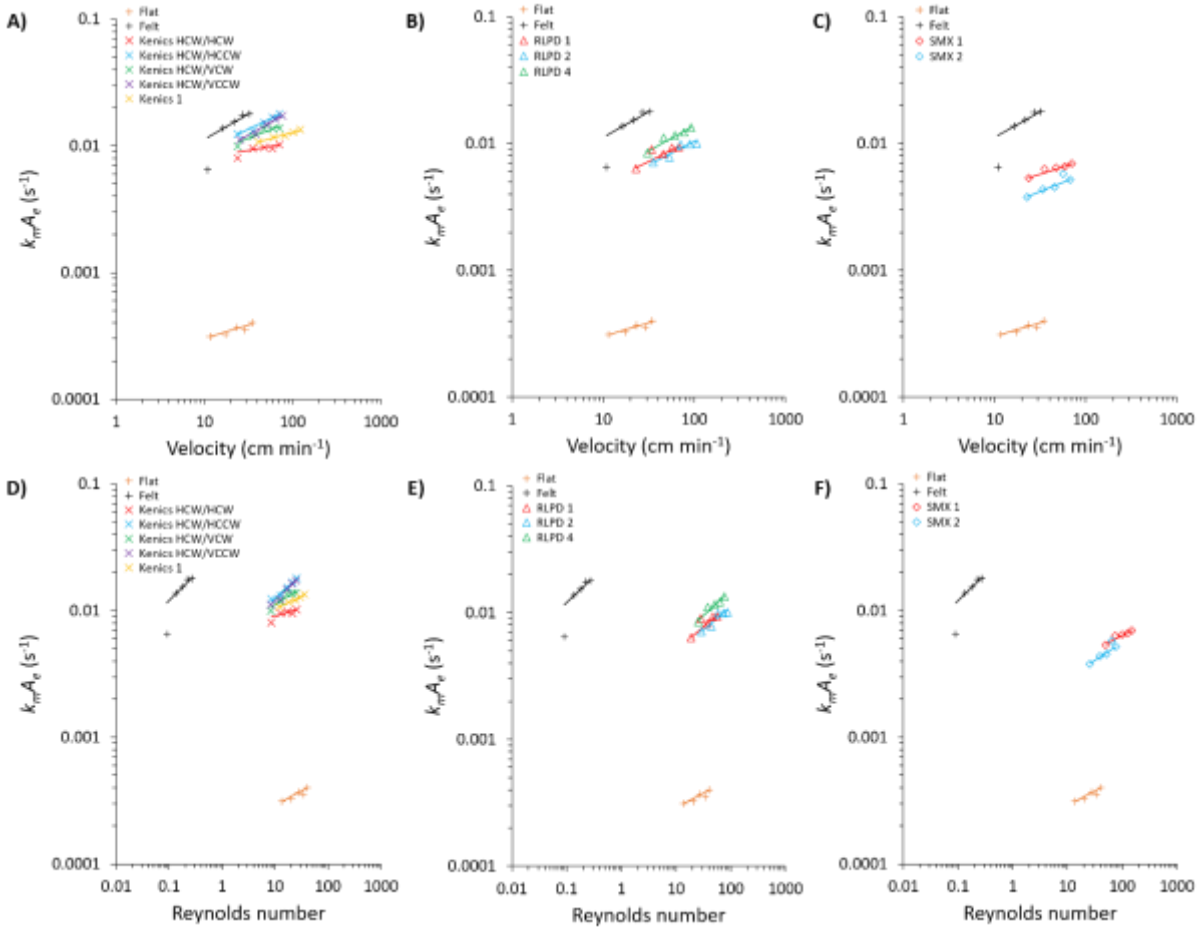

Fig. 4: The volumetric mass transfer coefficient (k_mA_e) as function of the mean electrolyte flow velocity: A) Kenics electrodes, B) RLPD electrodes and C) SMX electrodes. The volumetric mass transfer coefficient as function of the Reynolds number: D) Kenics electrodes, E) RLPD electrodes and F) SMX electrodes. The lines represent the fitted model (Eq. 6).

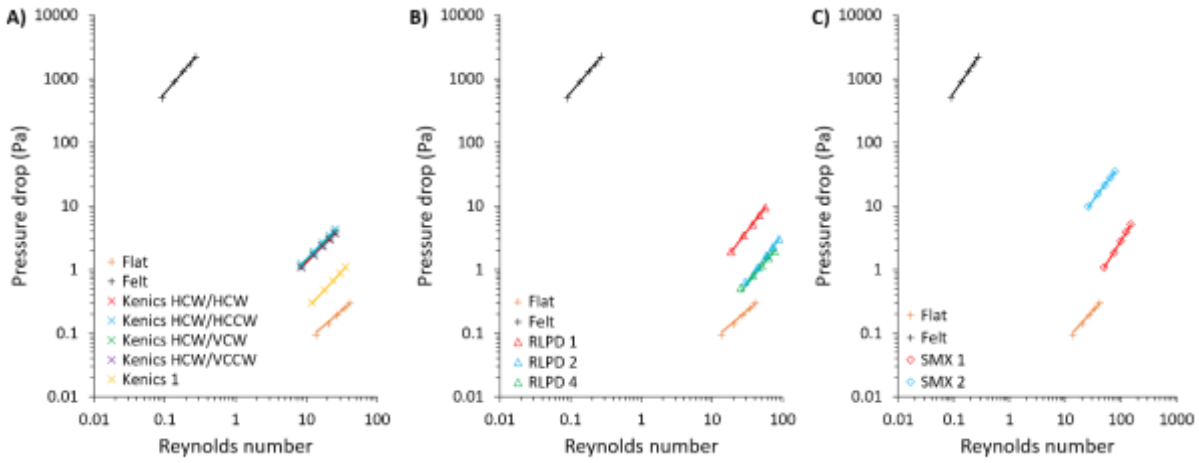

Fig. 5: The calculated pressure drop across the 3D electrode as function of the Reynolds number for various electrode geometries: A) Kenics electrode, B) RLPD electrode and C) SMX electrode. The lines represent the fitted model (Eq. 7).

While the mass transport properties of the felt electrode were higher than that of the structured 3D electrodes at equal electrolyte velocity, this was no longer the case at equal pressure drop (Fig. 6). Taking the pressure drop into account it can be observed that while the Kenics HCW/HCCW and Kenics HCW/VCCW electrodes yielded similar volumetric mass transfer coefficients than the felt electrode, the pressure drop was three orders of magnitude lower. Hence, when applying the same pumping power these Kenics electrodes outperform the commercial felt electrode. Comparing the Kenics electrodes (Fig. 6A) it can be observed that the electrodes consisting of two layers of helical elements yielded the highest volumetric mass transfer coefficient when the rotating direction of the two layers is opposite (i.e. clockwise (CW) and counter-clockwise (CCW)). When the rotating direction is similar (i.e. CW), the Kenics HCW/VCW electrode was able to match the Kenics 1 electrode regarding the volumetric mass transfer coefficient, although at the expense of a higher pressure drop. This can be explained by the fact that existence of preferential flow paths was somewhat counteracted by the opposite orientation (i.e. horizontal and vertical) between the two layers (see supporting information, Fig. S6). With the Kenics HCW/HCW electrode this was no

longer the case. The presence of preferential flow paths caused the electrode surface to be bypassed, resulting in the worst performance of all Kenics electrodes, even worse than the Kenics 1 electrode despite its larger surface area. This demonstrates once more the impact that the electrode geometry has on the electrochemical performance.

Comparing against the felt electrode, the RLPD electrodes all resulted in a lower volumetric mass transfer coefficient (Fig. 6B), however the pressure drop was still two to three orders of magnitude lower. Comparing the RLPD 4 electrode with the Kenics HCW/HCCW electrode (Fig. 6D) showed that the electrode performed similar. Moreover, by increasing the number of unit cells in the RLPD electrodes by decreasing the cross bar width, a positive impact on both the volumetric mass transfer coefficient and the pressure drop was observed, shifting the curves to the upper left corner. However, further decreasing the cross bar width resulted in a too weak mechanical electrode that was too prone for breakage during the manufacturing and reactor assembly process.

The SMX electrodes showed opposite behavior than the RLPD electrodes (Fig. 6C). By increasing the number of crossing elements (Fig. S4) the volumetric mass transfer coefficient decreased (SMX 2 < SMX 1) as the increase in electrode area could not compensate for the decrease in volumetric porosity, which lowered from 61.7 % to 38.2 %. This decrease in volumetric porosity increased the electrode volume (V_e) and as a result the product of the mass transfer coefficient (k_m) and the volumetric active area of the electrode (A_e) was lowered as the increase in k_m could not compensate for the decrease in A_e.

Like Eq. 6 Arenas et al. [21] also derived an empirical power law as function of the pressure drop across the electrode (Eq. 8).

$$k_m A_e = a_2 \Delta P^{b_2} \quad (8)$$

Here a_2 and b_2 are emperical variables that can be used to quantitatively characterize the different electrodes (Table S1). Variable a_2 is after the flat electrode the lowest for the felt electrode which can be explained by the high pressure drop the felt caused. Being in the laminar regime and to aid in comparing the flat and felt electrode against the structured 3D electrodes, the fitted empirical power law (Eq. 8) was extrapolated to the same pressure drop region as the structured 3D electrode results. For the felt electrode extrapolation was done towards lower pressure drops and thus lower Reynolds numbers, ensuring extrapolation was still in the laminar region. For the flat electrode extrapolation was done up to 10 Pa. At this pressure drop, from Eq. 7 *Re* was calculated and was equal to 1865. As shown by Tosun et al. [42] this is still lower than the critical Reynolds number, justifying the assumed laminar conditions. Due to the high pressure drop the felt electrode causes, the velocity at equal pressure drop will be much lower for the felt electrode than for all the other electrodes, negatively impacting the diffusion boundary layer and hence the mass transfer properties. Using structured 3D electrodes this pressure drop can be significantly reduced, without affecting the performance of the electrode.

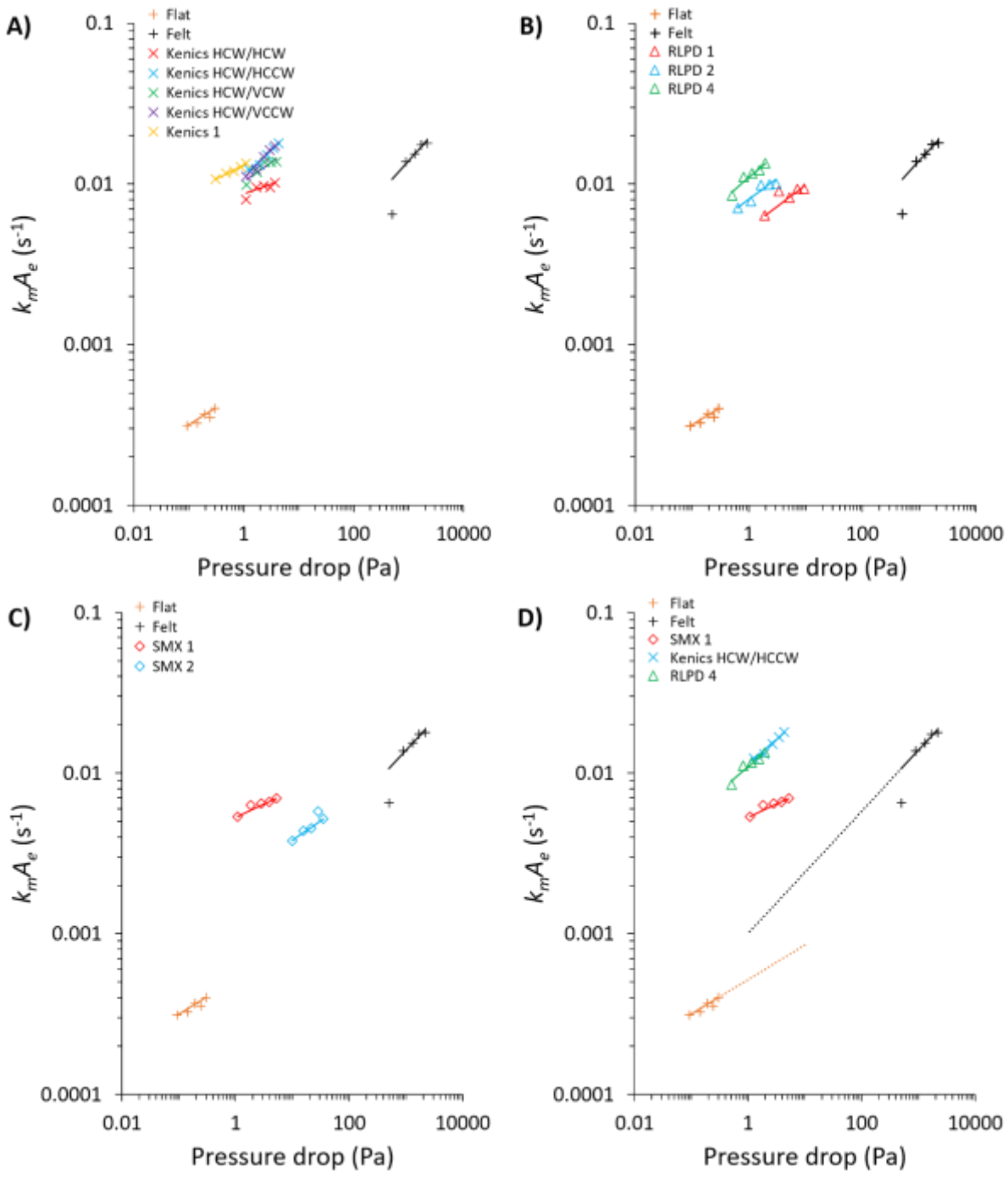

Fig. 6: The volumetric mass transfer coefficient (k_mA_e) as function of the pressure drop across the electrode channel: A) Kenics electrodes, B) RLPD electrodes, C) SMX electrodes and D) collection of the electrodes with the highest volumetric mass transfer coefficient. The dotted lines are extrapolations using the empirical variables of Eq. 8.

The energy required to pump liquids is directly linked to the pressure drop and described by the energy dissipation rate (γ) per mass unit of fluid (W kg^{-1}) (Eq. 9) [43].

$$\gamma = \frac{power\ input}{\rho\ V_f} = \frac{Q\ \Delta P}{\rho\ V_f} \tag{9}$$

Here V_f is the volume of fluid between the two points of pressure drop measurement. To achieve a volumetric mass transfer coefficient of 0.018 s^{-1} an energy dissipation rate of 213 mW kg^{-1} was required for the felt electrode whereas for the Kenics HCW/HCCW only an energy dissipation rate of 0.75 mW kg^{-1} was required. The corresponding power input for the felt electrode was 1.65 mW and for the Kenics HCW/HCCW 3.26 µW. This amounted to 5.4 % of the power consumed by the electrochemical ferri/ferro reaction for the felt electrode, whereas for the Kenics HCW/HCCW electrode this was only 0.01 %.

For the structured 3D electrodes and the flat electrode the volumetric active area of the electrode (A_e) was calculated from the CAD models (Inventor). With A_e known, the Sherwood number (Sh) was calculated from the limiting mass transfer coefficient (k_m) (Eq. 10).

$$Sh = \frac{k_m d_h}{D_m} \tag{10}$$

$$Sc = \frac{\mu}{\rho D_m} \tag{11}$$

Here D_m is the molecular diffusion coefficient which for ferricyanide is equal to 8.07 x10^{-8} m^2 s^{-1} [44]. In Fig. 7 the Sherwood number for the flat and structured 3D electrodes is given as function of the Reynolds number. Using Eq. 12 the Sherwood number could be expressed as function of the Reynolds and Schmidt number (Sc).

$$Sh = a_3 Re^{b_3} Sc^{1/3} \tag{12}$$

Here a_3 and b_3 are empirical variables (supporting information, Table S2). From Fig. 7 D it can be observed that the best Kenics, RLPD and SMX electrode all show higher Sherwood numbers than the flat electrode. Comparing the structured 3D electrodes in Fig. 7 D amongst one another it can be observed that they all result in similar Sherwood numbers. However, as stated by Walsh et al. [27] the electrode should not only result in a high mass transfer rate, but

also in a high volumetric surface area. To this end, the Kenics HCW/HCCW and RLPD 4 electrode showed the most promising results.

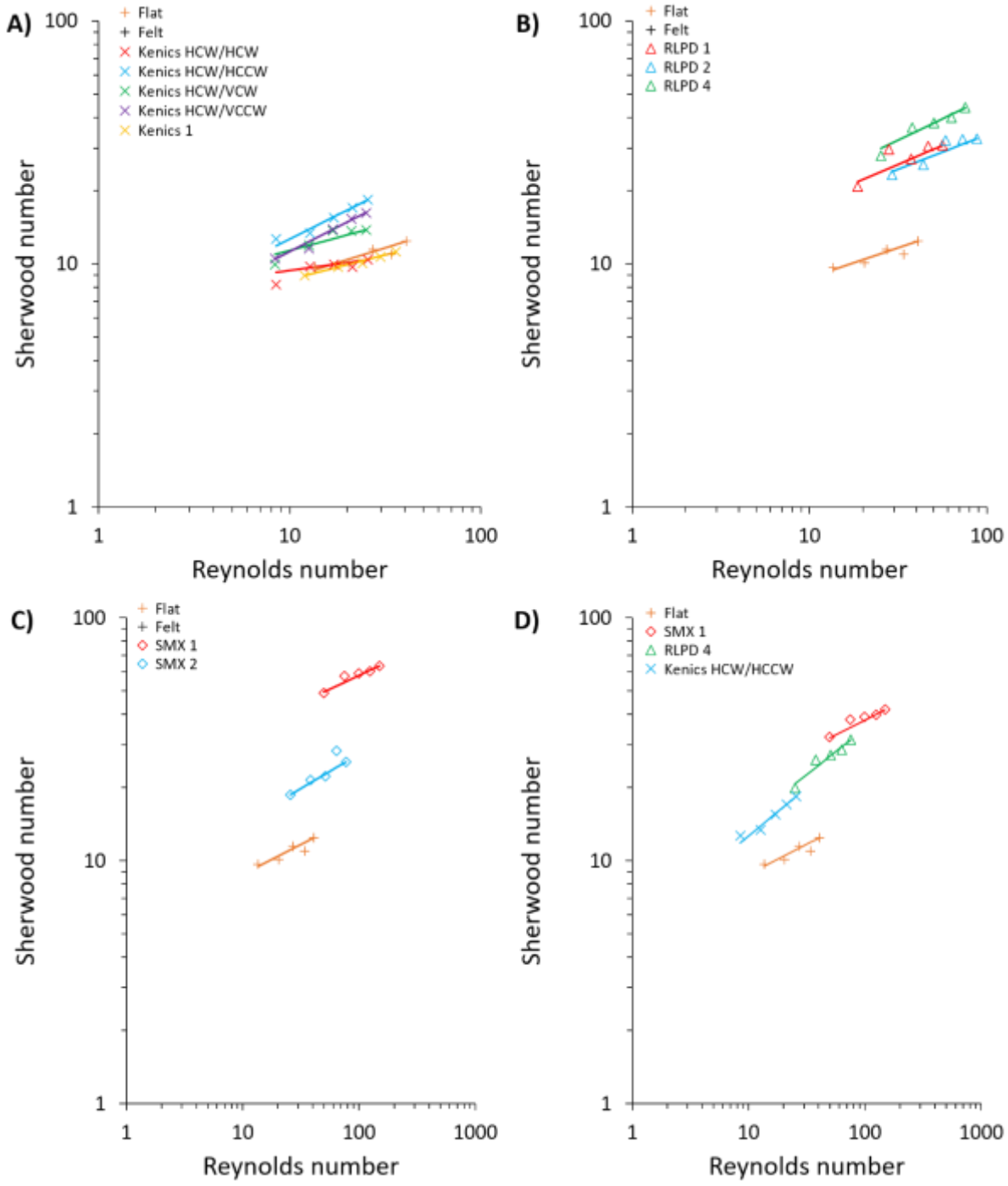

Fig. 7: Sherwood number as function of the Reynolds number: A) Kenics electrodes, B) RLPD electrodes, C) SMX electrodes and D) collection of the electrodes with the highest Sherwood number.

4. Conclusions

Structured 3D electrodes derived from static mixer designs were studied on their mass transfer properties as function of the pressure drop and compared against a commercial felt electrode and a common flat electrode. Being designed to minimize pressure drop all structured 3D electrodes showed a pressure drop that was one to two orders of magnitude lower than the felt electrode, significantly decreasing the pumping power. Despite this substantial lower pressure drop, the Kenics HCW/HCCW and the RLPD 4 electrode yielded similar volumetric mass transfer coefficients and hence similar electrochemical behavior as the felt electrode. Due to the regularly structured design these electrodes surpass the current state-of-the-art felt electrodes. The pressure drop at equal flow rates were much lower with the structured 3D electrodes compared to the felt electrode. With the continuous resolution improvement of additive manufacturing tools, this will allow in the future to increase the surface area of the structured 3D electrodes much more, improving their performance even further.

5. Acknowledgements

This project has received funding from the Research Foundation – Flanders (FWO) (Grant No. 53168). J. Hereijgers was supported through a postdoctoral fellowship (Grant No. 28761) of the Research Foundation – Flanders (FWO). J. Schalck was supported through a Baekeland grant of the Flanders Innovation & Entrepreneurship (VLAIO) (Grant No. HBC.2019.2163). The authors would like to thank Simon Himpe for assisting with the measurements.

6. References

[1] T. Brinkmann, G.G. Santonja, F. Schorcht, S. Roudier, L.D. Sancho, Best Available Techniques (BAT) Reference Document for the production of chlor-alkali, 2014.

doi:10.2791/13138.

[2] N.G. Carpenter, E.P.L. Roberts, Mass transport and residence time characteristics of an oscillatory flow electrochemical reactor, Inst. Chem. Eng. Symp. Ser. 77 (1999) 309–318. doi:10.1205/026387699526115.

[3] M. Griffiths, C.P. de León, F.C. Walsh, Mass transport in the rectangular channel of a filter-press electrolyzer (the FM01-LC reactor), AIChE J. 51 (2005) 682–687. doi:10.1002/aic.10311.

[4] F.F. Rivera, C.P. De León, J.L. Nava, F.C. Walsh, The filter-press FM01-LC laboratory flow reactor and its applications, Electrochim. Acta. 163 (2015) 338–354. doi:10.1016/j.electacta.2015.02.179.

[5] F.F. Rivera, C.P. De León, F.C. Walsh, J.L. Nava, The reaction environment in a filter-press laboratory reactor: the FM01-LC flow cell, Electrochim. Acta. 161 (2015) 436–452. doi:10.1016/j.electacta.2015.02.161.

[6] F.A. Rodríguez, E.P. Rivero, I. González, Electrogeneration of Active Chlorine in a Filter-Press-Type Reactor Using a New Sb2O5 Doped Ti/RuO2-ZrO2 Electrode: Indirect Indigoid Dye Oxidation, Int. J. Chem. React. Eng. 15 (2017). doi:10.1515/ijcre-2016-0095.

[7] B. Taylor, From test stations to commercialization within a decade at Hydrogenics, Fuel Cells Bull. 2004 (2004) 10–14. doi:10.1016/S1464-2859(04)00153-1.

[8] B. De Mot, J. Hereijgers, M. Duarte, T. Breugelmans, Influence of flow and pressure distribution inside a gas diffusion electrode on the performance of a flow-by CO2 electrolyzer, Chem. Eng. J. 378 (2019) 122224. doi:10.1016/j.cej.2019.122224.

[9] C.J. Brown, D. Pletcher, F.C. Walsh, J.K. Hammond, D. Robinson, Local mass transport effects in the FM01 laboratory electrolyser, J. Appl. Electrochem. 22 (1992) 613–619. doi:10.1007/BF01092609.

[10] J. González-García, A. Frías, E. Expósito, V. Montiel, A. Aldaz, J.A. Conesa, Characterization of an electrochemical pilot-plant filter-press reactor by hydrodynamic and mass transport studies, Ind. Eng. Chem. Res. 39 (2000) 1132–1142. doi:10.1021/ie990351q.

[11] Á. Frías-Ferrer, J. González-García, V. Sáez, C.P. de León, F.C. Walsh, The effects of manifold flow on mass transport in electrochemical filter-press reactors, AIChE J. 54 (2008) 811–823. doi:10.1002/aic.11426.

[12] L.F. Castañeda, F.C. Walsh, J.L. Nava, C. Ponce de León, Graphite felt as a versatile electrode material: Properties, reaction environment, performance and applications, Electrochim. Acta. 258 (2017) 1115–1139. doi:10.1016/j.electacta.2017.11.165.

[13] S.J.P. Romkes, F.M. Dautzenberg, C.M. van den Bleek, H.P.A. Calis, CFD modelling and experimental validation of particle-to-fluid mass and heat transfer in a packed bed at very low channel to particle diameter ratio, Chem. Eng. J. 96 (2003) 3–13. doi:10.1016/j.cej.2003.08.026.

[14] S. Bu, J. Yang, Q. Dong, Q. Wang, Experimental study of flow transitions in structured packed beds of spheres with electrochemical technique, Exp. Therm. Fluid Sci. 60 (2015) 106–114. doi:10.1016/j.expthermflusci.2014.09.001.

[15] L.F. Arenas, C. Ponce de León, F.C. Walsh, Pressure drop through platinized titanium porous electrodes for cerium-based redox flow batteries, AIChE J. 64 (2018) 1135–1146. doi:10.1002/aic.16000.

[16] D. Bryans, V. Amstutz, H. Girault, L. Berlouis, Characterisation of a 200 kW/400 kWh Vanadium Redox Flow Battery, Batteries. 4 (2018) 54. doi:10.3390/batteries4040054.

[17] C.-Y. Lee, A.C. Taylor, A. Nattestad, S. Beirne, G.G. Wallace, 3D Printing for Electrocatalytic Applications, Joule. 3 (2019) 1835–1849. doi:10.1016/j.joule.2019.06.010.

[18] L.F. Arenas, F.C. Walsh, C.P. de León, 3D-Printing of Redox Flow Batteries for Energy Storage: A Rapid Prototype Laboratory Cell, ECS J. Solid State Sci. Technol. 4 (2015) P3080–P3085. doi:10.1149/2.0141504jss.

[19] J. Hereijgers, J. Schalck, J. Lölsberg, M. Wessling, T. Breugelmans, Indirect 3D Printed Electrode Mixers, ChemElectroChem. 6 (2019) 378–382. doi:10.1002/celc.201801436.

[20] J. Lölsberg, O. Starck, S. Stiefel, J. Hereijgers, T. Breugelmans, M. Wessling, 3D-Printed Electrodes with Improved Mass Transport Properties, ChemElectroChem. 4 (2017) 3309–3313. doi:10.1002/celc.201700662.

[21] L.F. Arenas, C.P. de León, F.C. Walsh, Mass transport and active area of porous Pt/Ti electrodes for the Zn-Ce redox flow battery determined from limiting current measurements, Electrochim. Acta. 221 (2016) 154–166. doi:10.1016/j.electacta.2016.10.097.

[22] Q. Wang, Z.G. Qu, Z.Y. Jiang, W.W. Yang, Experimental study on the performance of a vanadium redox flow battery with non-uniformly compressed carbon felt electrode, Appl. Energy. 213 (2018) 293–305. doi:10.1016/j.apenergy.2018.01.047.

[23] K.J. Myers, E.E. Janz, N. Cathie, M.A. Jones, Employ Static Mixers for Process Intensification, CEP Mag. (n.d.).

[24] H.E.H. Meijer, M.K. Singh, P.D. Anderson, On the performance of static mixers: A quantitative comparison, Prog. Polym. Sci. 37 (2012) 1333–1349. doi:10.1016/j.progpolymsci.2011.12.004.

[25] C. Ponce de León, R.W. Field, On the determination of limiting current density from uncertain data, J. Appl. Electrochem. 30 (2000) 1087–1090. doi:10.1023/A:1004015617522.

[26] D. Pletcher, I. Whyte, F.C. Walsh, J.P. Millington, Reticulated vitreous carbon

cathodes for metal ion removal from process streams part I: Mass transport studies, J. Appl. Electrochem. 21 (1991) 659–666. doi:10.1007/BF01034042.

[27] F. Walsh, G. Reade, Design and performance of electrochemical reactors for efficient synthesis and environmental treatment. Part 1. Electrode geometry and figures of merit, Analyst. 119 (1994) 791. doi:10.1039/an9941900791.

[28] F.F. Rivera, C.P. de León, F.C. Walsh, J.L. Nava, The reaction environment in a filter-press laboratory reactor: the FM01-LC flow cell, Electrochim. Acta. 161 (2015) 436–452. doi:10.1016/j.electacta.2015.02.161.

[29] A. Fetyan, J. Schneider, M. Schnucklake, G.A. El-Nagar, R. Banerjee, N. Bevilacqua, R. Zeis, C. Roth, Comparison of Electrospun Carbon−Carbon Composite and Commercial Felt for Their Activity and Electrolyte Utilization in Vanadium Redox Flow Batteries, ChemElectroChem. 6 (2019) 6. doi:10.1002/celc.201801706.

[30] D. Pauwels, B. Geboes, J. Hereijgers, D. Choukroun, K. De Wael, T. Breugelmans, The application of an electrochemical microflow reactor for the electrosynthetic aldol reaction of acetone to diacetone alcohol, Chem. Eng. Res. Des. 128 (2017) 205–213. doi:10.1016/j.cherd.2017.10.014.

[31] S. Langlois, F. Coeuret, Flow-through and flow-by porous electrodes of nickel foam. I. Material characterization, J. Appl. Electrochem. 19 (1989) 43–50. doi:10.1007/BF01039388.

[32] J. Newman, Simultaneous reactions at disk and porous electrodes, Electrochim. Acta. 22 (1977) 903–911. doi:10.1016/0013-4686(77)85002-0.

[33] M.S. El-Deab, M.M. Saleh, B.E. El-Anadouli, B.G. Ateya, Electrochemical removal of lead ions from flowing electrolytes using packed bed electrodes, J. Electrochem. Soc. 146 (1999) 208–213. doi:10.1149/1.1391588.

[34] H.E.H. Meijer, M.K. Singh, P.D. Anderson, On the performance of static mixers: A

quantitative comparison, Prog. Polym. Sci. 37 (2012) 1333–1349. doi:10.1016/j.progpolymsci.2011.12.004.

[35] J.M. Zalc, E.S. Szalai, F.J. Muzzio, Characterization of Flow and Mixing in an SMX Static Mixer, 48 (2002) 427–436.

[36] K. Hirech, A. Arhaliass, J. Legrand, Experimental Investigation of Flow Regimes in an SMX Sulzer Static Mixer, (2003) 1478–1484.

[37] D.M. Hobbs, F.J. Muzzio, Chemical Engineering Reynolds number effects on laminar mixing in the Kenics static mixer, 70 (1998) 93–104.

[38] Z. Jaworski, P. Pianko-Oprych, Two-phase laminar flow simulations in a Kenics static mixer: Standard Eulerian and Lagrangian approaches, Chem. Eng. Res. Des. 80 (2002) 910–916. doi:10.1205/026387602321143462.

[39] V. Geraldes, V. Semiano, M. Norberta de Pinho, Flow management in nanofiltration spiral wound modules with ladder-type spacers, J. Memb. Sci. 203 (2002) 87–102. doi:10.1016/S0376-7388(01)00753-0.

[40] D.L. Marchisio, A.A. Barresi, R.O. Fox, Simulation of Turbulent Precipitation in a Semi-batch Taylor-Couette Reactor Using CFD, AIChE J. 47 (2001) 664–676. doi:10.1002/aic.690470314.

[41] M.A. Sandoval, R. Fuentes, F.C. Walsh, J.L. Nava, C.P. de León, Computational fluid dynamics simulations of single-phase flow in a filter-press flow reactor having a stack of three cells, Electrochim. Acta. 216 (2016) 490–498. doi:10.1016/j.electacta.2016.09.045.

[42] I. Tosun, D. Uner, C. Ozgen, Critical Reynolds number for Newtonian flow in rectangular ducts, Ind. Eng. Chem. Res. 27 (1988) 1955–1957. doi:10.1021/ie00082a034.

[43] L. Falk, J.M. Commenge, Performance comparison of micromixers, Chem. Eng. Sci.

65 (2010) 405–411. doi:10.1016/j.ces.2009.05.045.

[44] E. Tourwé, T. Breugelmans, R. Pintelon, A. Hubin, Extraction of a quantitative reaction mechanism from linear sweep voltammograms obtained on a rotating disk electrode. Part II: Application to the redoxcouple, J. Electroanal. Chem. 609 (2007) 1–7. doi:10.1016/j.jelechem.2006.12.019.